

# Surface-Normal Free-Space Beam Projection via Slow-Light Standing-Wave Resonance Photonic Gratings

Alexander Yulaev, Daron A. Westly, and Vladimir A. Aksyuk\*

Cite This: <https://doi.org/10.1021/acsp Photonics.2c00422>

Read Online

ACCESS |



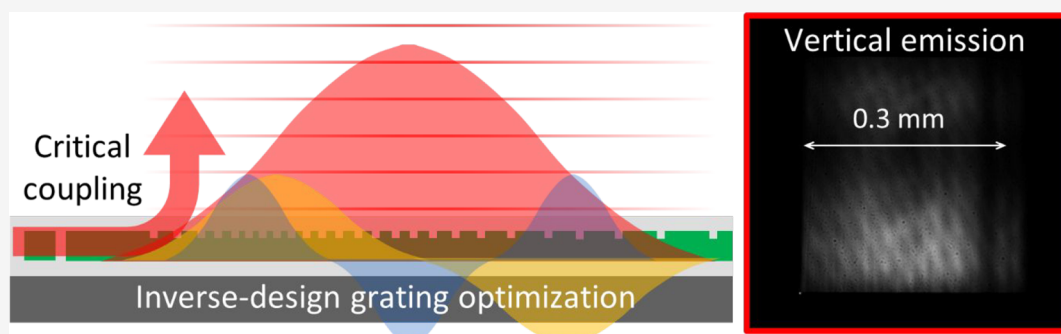
Metrics &amp; More



Article Recommendations



Supporting Information



**ABSTRACT:** On-chip grating couplers directly connect photonic circuits to free-space light. The commonly used photonic gratings have been specialized for small areas, specific intensity profiles, and nonvertical beam projection. This falls short of the precise and flexible wavefront control over large beam areas needed to empower emerging integrated miniaturized optical systems that leverage volumetric light–matter interactions, including trapping, cooling, and interrogation of atoms, bio- and chemi- sensing, and complex free-space interconnect. The large coupler size challenges general inverse design techniques, and solutions obtained by them are often difficult to physically understand and generalize. Here, by posing the problem to a carefully constrained computational inverse-design algorithm capable of large area structures, we discover a qualitatively new class of grating couplers. The numerically found solutions can be understood as coupling an incident photonic slab mode to a spatially extended slow-light (near-zero refractive index) region, backed by a reflector. The structure forms a spectrally broad standing wave resonance at the target wavelength, radiating vertically into free space. A reflectionless adiabatic transition critically couples the incident photonic mode to the resonance, and the numerically optimized lower cladding provides 70% overall theoretical conversion efficiency. We have experimentally validated an efficient surface normal collimated emission of  $\approx 90 \mu\text{m}$  full width at half-maximum Gaussian at the thermally tunable operating wavelength of  $\approx 780 \text{ nm}$ . The variable-mesh-deformation inverse design approach scales to extra large photonic devices, while directly implementing the fabrication constraints. The deliberate choice of smooth parametrization resulted in a novel type of solution, which is both efficient and physically comprehensible.

**KEYWORDS:** PIC, grating coupler, optimization, vertical coupling

## INTRODUCTION

The ability to project arbitrarily shaped, wide, collimated beams directly from a photonic chip to free space is key to realizing miniaturized chip-scale devices for optical spectroscopy,<sup>1</sup> atom interrogation and trapping,<sup>2–6</sup> chemi- and biosensing,<sup>7–12</sup> and optical communications.<sup>13</sup> To achieve the desired free-space light–matter interaction, a photonic device has to efficiently couple to free-space beams with well-defined polarization, intensity, and phase profiles propagating over millimeter-long distances.

Small-scale gratings are widely employed in photonics to convert submicrometer wide waveguide modes to free-space radiation,<sup>14–21</sup> primarily for fiber coupling. The major drawback of conventional grating couplers is their limited ability to match photonics to spatially extended free-space

modes, typically covering only  $\approx 100\times$  in mode field diameter expansion. The typical narrow photonic emitted free-space beams have a relatively short Rayleigh range of  $\approx 100 \mu\text{m}$ , and their fast divergence due to diffraction makes them unsuitable for implementing hybrid 3D microsystems, where light–matter interaction occurs in volume rather than at surfaces.

Exciting recent developments in designing large photonic platforms such as a  $300 \mu\text{m}$  long extreme mode converter,<sup>22</sup>

**Special Issue:** Optimized Photonics and Inverse Design

**Received:** March 15, 2022

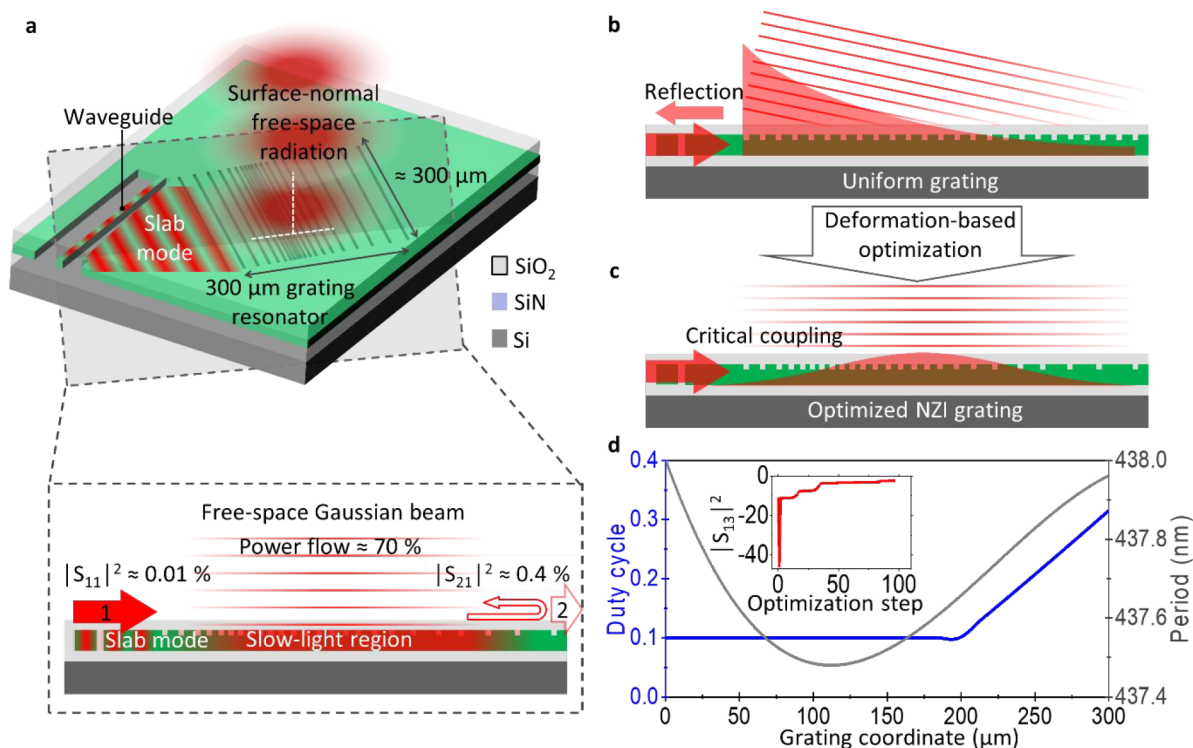


**Figure 1.** Resonant photonic grating design. (a) 3D Schematic illustrating the principal of operation. The dash box depicts the cross-sectional cartoon of the resonant grating performance. First, a waveguide single mode expands across the evanescent gap forming a collimated slab wave. Next, the apodized grating projects a surface-normal wide collimated beam into free-space from a slab mode. Arrows with 1 and 2 point out the incident and transmitted slab waves, respectively. (b) and (c) show a uniform and an apodized NZI grating, respectively. The latter is optimized by deforming the uniform grating, spatially varying the period and DC to maximize slab-to-free-space coupling. (d) The optimized DC (blue) and period (gray) along the grating found using the inverse-design FEM. The inset depicts the optimization evolution:  $|S_{13}|^2$ , that is, slab-to-free-space coupling efficiency in dB units relative to unity vs optimization iteration.

metasurface-integrated grating couplers,<sup>23,24</sup> weakly scattering gratings in thin SiN<sub>x</sub> layers,<sup>25</sup> and the grating Segmented Planar Imaging Detector for Electro-optical Reconnaissance (SPIDER) telescope<sup>26</sup> open up large sizes with control over intensity, phase and polarization state. They include reciprocal coupling of wide collimated or high-numerical-aperture focusing free-space beams with well-controlled properties to photonic modes for trapping and interrogating chip-scale atomic systems and realizing interferometric imaging systems based on photonic integrated circuits.

Beams projected normally to the photonic chip surface are particularly desired for a range of applications to simplify optical alignment and integration with other planar components and to reduce packaging costs. However, vertical emission of spatially broad free-space beams remains particularly inefficient due to the intrinsic symmetry of vertically etched grating structures. This difficulty is apparent in the reciprocal problem setting, where an incident surface-normal free-space beam is evenly coupled to the left- and right-propagating grating modes in the locally left–right symmetric grating. Our previous approach,<sup>22</sup> although allows for projecting >100 μm wide collimated Gaussian beam, becomes problematic once constrained to emit vertically. The problem can be mitigated using optically thick structures capable of distinguishing up from down at the expense of more complicated processing that requires high accuracy alignment<sup>27</sup> or slanted etching.<sup>28,29</sup>

Dispersion engineering based on slow-light in plasmonic and photonic systems, which is typically used to realize time

domain processing, ultracompact optical buffers, optical delay lines, and all-optical signal processors<sup>30–32</sup> can help cope with both a strong chromatic dispersion and significant slab mode back reflection while maintaining the surface-normal light projection. Moreover, lowering and controlling a waveguide group velocity is a practical tool for modulating light intensity. Plasmonic waveguides, quasi-periodic plasmonic nanostructures, and their hybrids with photonic waveguides have been proposed to slow down or even stop light waves.<sup>33–35</sup> Unfortunately, plasmonic systems are too intrinsically lossy to be practically implemented. Near-zero index (NZI) photonics, another class of structured dielectrics, enabling the static light due to decoupling of spatial and temporal fields, exhibit exotic phenomena such as light tunneling, perfect phase matching, light trapping, highly directed emission, and enhanced nonlinearities that can also facilitate tailoring of light properties.<sup>36–39</sup>

Here, we utilize a deformation-based inverse design method, a recently introduced qualitatively different approach for solving the problem, to devise a 300 μm long photonic grating capable of projecting a 90 μm full width at half-maximum (fwhm), collimated free-space beam exactly normally to the surface. Distinct from the inverse-design algorithms relying on optimizing the material properties in a design region, we make use of spatially varying induced deformations applied to a uniform grating, which is essential to handle photonic structures spanning over 600 waves. The obtained solution contains a structured slow-light NZI region supporting spatially broad resonances, including the single-peak funda-

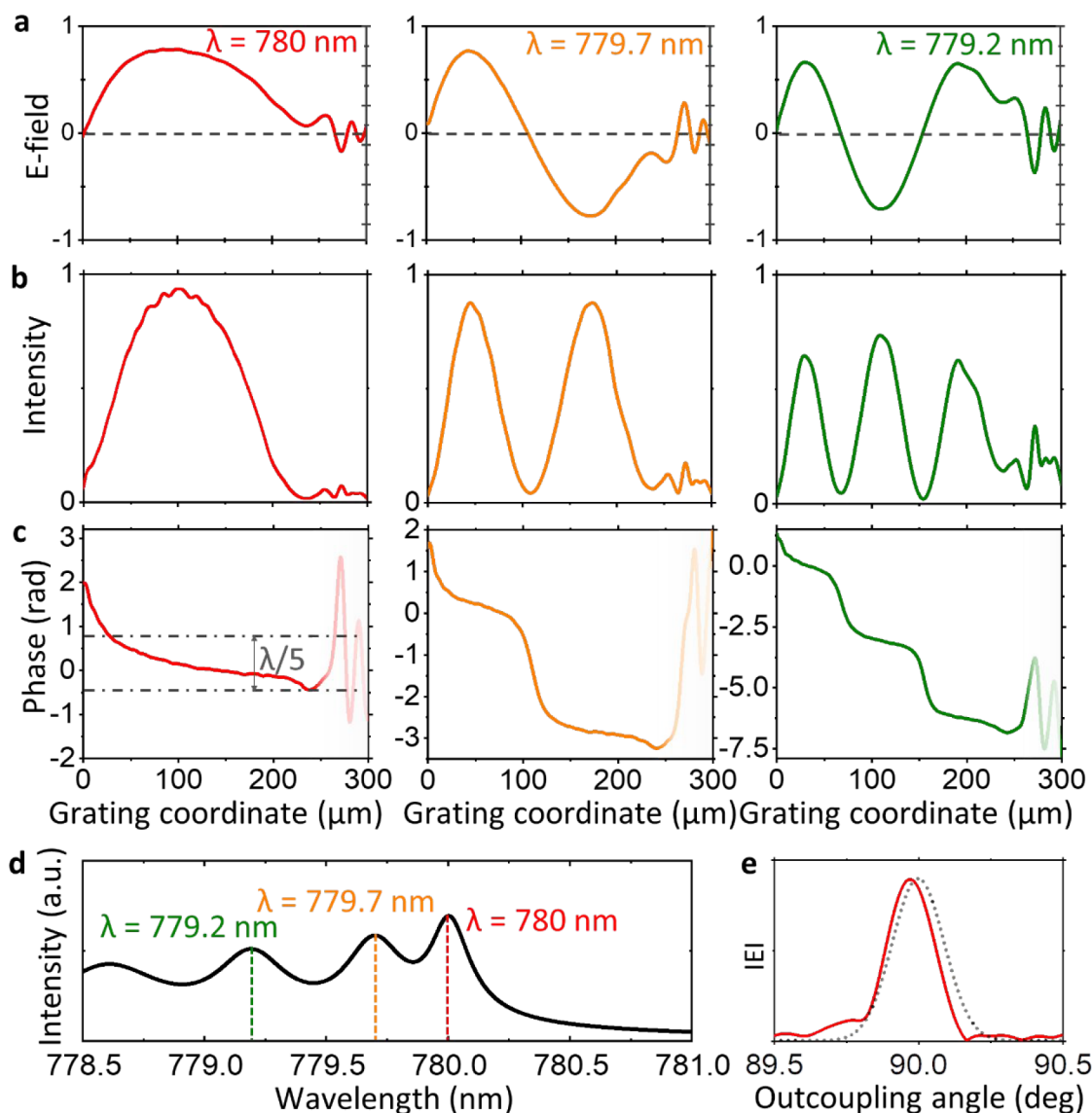


**Figure 2.** Simulated resonant grating performance. (a), (b), and (c) depict electric field, intensity profiles, and phase of the first three spatially broad resonant modes supported in the optimized grating and projected in free space at  $\lambda = 780$ ,  $779.7$ , and  $779.2$  nm. The grating extends from 0 to  $300 \mu\text{m}$ . The complex electric field is sampled  $3 \mu\text{m}$  above the grating surface. (d) Outcoupled free-space power from the grating vs laser wavelength. (e) Far-field distribution of the fundamental mode vs outcoupling angle (solid curve). The dotted curve depicts the Fourier transformed Gaussian fit of the fundamental mode assuming a perfectly collimated surface normal beam projection.

mental half-wave and the higher-order standing waves, observed by their characteristic free-space radiation patterns. The input light is critically coupled to the resonances via a reflection-free adiabatic transition designed by the algorithm, achieving full impedance matching between the photonic and the free-space radiation mode. Our photonic device bridges the  $10^5$  area mismatch between the photonic waveguide and surface-normal free-space radiation with 70% theoretical conversion efficiency. We have experimentally confirmed efficient, surface-normal collimated emission, where each mode can be readily selected by tuning either the laser wavelength or the device temperature. These results demonstrate the ability of intelligently parametrized inverse design to find novel classes of solutions that are physically comprehensible and, therefore, can be generalized and adapted for different specific application requirements, for example, different mode shapes and wavelength ranges.

## RESULTS

**Design of the Resonant Grating.** We follow the commonly used approach for coupling of a highly confined waveguide mode to a surface-normal wide collimated radiation by first converting the waveguide mode into a wide, collimated, vertically confined slab mode, followed by outcoupling of the slab mode to free space. The choice of  $\text{Si}_3\text{N}_4$  as a waveguide core material both provides high refractive index contrast and covers a broad spectral range, including visible wavelengths, at low losses. As illustrated in Figure 1a, for the first stage we use a photonic evanescent wave expander with a precisely designed gap between a single-mode waveguide and a slab, as reported previously.<sup>22,23,40</sup> The focus of this manuscript is the second stage, which uses the numerically optimized grating supporting a spatially broad standing wave resonance for coupling the slab mode to free space.

Our solution strategy relies on an automated inverse design—a fast and general approach of searching for optical structures that optimize functional performance, which has recently revolutionized the computational photonic methods.<sup>41,42</sup> To obtain the grating structure, we use a gradient-based adjoint optimization algorithm combined with the finite element method (FEM). We set a cost function to maximize the coupling efficiency from a transverse electric (TE)-polarized photonic wave to a surface-normal, 100  $\mu\text{m}$  waist, collimated free-space Gaussian beam. Instead of spatially varying material properties, we induce smooth deformations of an initially uniform period grating.<sup>33</sup> The deformation is implemented by a continuous motion of mesh elements, resulting in the continuous positioning of the grating groove walls with arbitrary resolution independently of the mesh size and without remeshing. Owing to the wide and collimated input (slab) and output (free-space) modes, the grating modeling is reduced from a 3D to a computationally simpler 2D TE wave scattering problem. Another advantage of the deformation-based method is a binary materials choice throughout the optimization, which does not require forcing intermediate solutions of the continuously varying materials properties to satisfy the binary material constraint.

Any arbitrary grating geometry can be achieved, topologically, by continuously deforming an initially uniform periodic grating. Given the slowly varying Gaussian function as the desired free-space beam profile, we further restrict the deformations to the grating period and duty cycle (DC) expressed by independent third and fourth order polynomials with coefficients that serve as the control parameters. Here the grating is deformed globally according to the varying period, and then each period is further deformed locally to achieve the desired spatially varying duty cycle. This parametrization restricts the solutions to smoothly varying duty cycles and periods. While this solution space effectively excludes more exotic situations, such as having more than a single groove in any given period, this is a deliberate choice aimed at obtaining optimized solutions that are easier to physically understand. During inverse-design optimization, we allow both the groove depth and bottom  $\text{SiO}_2$  cladding thickness to vary via vertical deformation, while keeping each of them uniform across the device. The substrate is the only object breaking the up–down symmetry in the problem. It is known that efficiency can be improved further by using more complex up–down asymmetric designs, such as a double-side grating.<sup>27</sup> However, such designs are more complex to fabricate and, while within the scope of our inverse-design approach, they are not considered in this work. Due to practical nanofabrication limits, we constrain the minimal DC to 0.1.

Our method of optimization of geometry by deformation for specific single-frequency wave scattering objectives is not specific for two dimensions and can be used with 3D scattering problems, provided sufficient computational resources (memory, processing speed) are utilized for the, typically, larger problem size. Regardless of dimensionality, the class of solutions that can be found is limited to those achieved by smooth deformations of the initial device geometry without strongly distorting the original mesh that is being deformed. This rules out using this technique where changes in the device topology, such as adding through-holes, are contemplated.

Starting from the uniform duty cycle and period (Figure 1b), the inverse design algorithm explores the space of parametrized gradual deformations without further human intervention and

finds an optimized grating geometry (Figure 1c) that emanates an  $\approx 118 \mu\text{m}$  fwhm surface-normal collimated beam (the red curves in Figure 2a,b). The resulting DC and period profiles can be qualitatively understood from the band diagrams (BDs) corresponding to three locations on the grating, beginning, middle and end, with their respective periods and duty cycles. At the grating coordinate  $x \approx 100 \mu\text{m}$  the grating's stop-band edge approaches the frequency of the incident light (Figure S7(ii)). First, to minimize reflection and maximize coupling of the slab wave into the photonic structure, the grating parameters vary smoothly on the input to provide full impedance matching between the slab mode and the grating (Figure 1d). The period adiabatically changes within the subnanometer range from the  $x = 0 \mu\text{m}$ , where a slab wave enters the grating to the middle of the device, decelerating the leaky grating mode (Figure S7(i)) due to the bandgap edge proximity and hence increasing the light intensity due to the group index growth (Figure S8). Next, both the DC and the period ramp at the opposite end to reflect the remaining grating power backward (Figure S7(iii)). This forms a slow-light standing wave with a single half-period of  $\approx 200 \mu\text{m}$  at the optimization wavelength. The grating mode at the top branch of the band diagram is a leaky mode (Figures S7 and S8), efficiently coupling to free-space, and the standing wave nature ensures surface-normal radiation. This is very distinct from the standing wave regime formed by two conservative grating modes propagating in opposite directions due to the Bragg reflection or photonic crystal localized resonances. While the phase is maintained constant for a loss-less medium, adding a lossy radiative channel moves the eigenvalues of photonic modes from real-value to complex-value domain. In this case, the radiation fails to keep the uniform phase across the free-space beam, and the emission becomes significantly off-normal.

Overall, the optimized photonic structure provides the critical coupling of the slab wave to the radiating resonant grating, resulting in only  $\approx 0.01\%$  power slab wave reflection from the grating,  $\approx 0.4\%$  power slab wave transmission, and  $\approx 70\%$  conversion to the upward-pointing free-space beam (Figure 1a) numerically modeled at the optimization wavelength. Because the slab mode in a thin, partially etched grating layer radiates almost equal powers up and down and given only partial reflectivity of the underlying oxide-silicon interface, optical losses into the Si substrate cannot be fully eliminated by only optimizing the lower oxide cladding thickness.

By numerically examining the device transmission spectrum to free space, we see the bandgap, the fundamental resonance (quality factor of  $\approx 3000$ ), and other standing-wave resonances at blue detuned wavelengths, separated by regions of reduced emission, as shown in Figure 2. Although the photonic emitter is inverse designed to maximize only the conversion efficiency at a single wavelength of the fundamental mode (780 nm), the other resonances demonstrate peak outcoupling power values that are lower but comparable to that of the fundamental (Figure 2d). The resonances' field and intensity profiles show the integer numbers of half-periods along the grating (Figure 2a,b), while their standing wave nature is confirmed by the nearly flat phase profile for the fundamental and the piece-wise flat phase profiles for the higher order resonances in Figure 2c. Hence, the apodized grating operates in a NZI regime, where fields' spatial distribution decouples from the temporal field variation and acquires a static-like character.<sup>38</sup> All the modes are collimated and outcoupled close to the chip's surface-normal, demonstrating near-zero angle refraction typical for

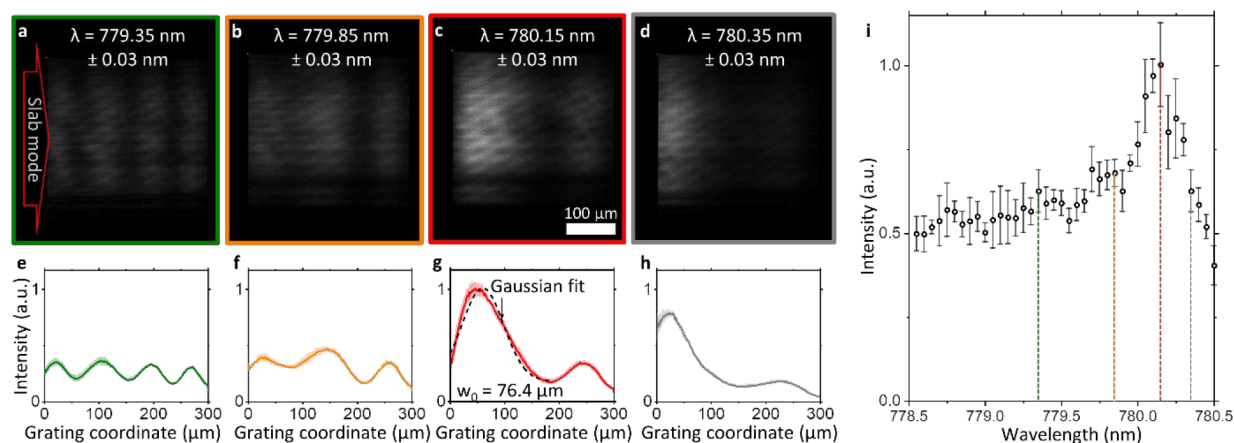


**Figure 3.** Experimental spectroscopic characterization of the resonant gratings. (a–d) Top-view optical images of the free-space beam projected from the photonic grating at  $779.35 \pm 0.03 \text{ nm}$ ,  $779.85 \pm 0.03 \text{ nm}$ ,  $780.15 \pm 0.03 \text{ nm}$ , and  $780.35 \pm 0.03 \text{ nm}$  wavelength depicting the third, second, and fundamental resonant modes, and the intensity profile detuned into the band gap, respectively. Wavelength uncertainties are one standard deviation of the multiple calibrated laser wavelength measurements across the range from 778.3 to 781.3 nm. (e–h) Intensity profiles corresponding to images depicted in panels (a)–(d). Dotted line in panel (g) is a Gaussian fit. (i) Outcoupled free-space power from the grating, normalized to its maximum vs laser wavelength. Error bars are single standard deviations of the data obtained by equally dividing the images into five subdomains along the grating width.

NZI systems<sup>37</sup> (Figures 2c and S1). The similar NZI mode has been demonstrated earlier,<sup>36</sup> but manifesting a zero-phase index and a finite group index, that is, a Dirac cone rather than the apodized bandgap in our resonant grating. Figure 2e depicts the angular dependence of the far-field free-space electric field (solid curve) and the Fourier transformed Gaussian fit of the fundamental mode (dotted curve) assuming a perfectly collimated surface-normal beam projection. From the far-field analysis, we infer that the free-space beam coupled out from the fundamental grating standing wave is diffraction limited and emanating very close to a surface normal.

**Resonant Grating Performance.** The experimental far-field intensity profiles of the projected free-space beam depict the single-peak (fundamental) mode at  $780.15 \pm 0.03 \text{ nm}$  wavelength (Figure 3c,g) and other blue-shifted multiple-peak patterns (Figure 3a,b,e,f). As expected, red-wavelength detuning falls into a band gap (Figure 3d,h). The discrepancy between experimental and simulated data is attributed to fabrication imperfections. Since the experimental grating parameters, such as slab thickness, grating DC, depth, and period, define the accuracy of a resonant mode by adjusting the fabrication process we can tune the device operating wavelength.

The experimental free-space intensity profiles shown in Figure 3e–h correspond to the integrated fundamental, second and third resonant modes, and the intensity profile in the band gap (Figure 3a–d) projected from the resonant grating at  $780.15 \pm 0.03 \text{ nm}$ ,  $779.85 \pm 0.03 \text{ nm}$ ,  $779.35 \pm 0.03 \text{ nm}$ , and  $780.35 \pm 0.03 \text{ nm}$  wavelengths, respectively. The experimental data qualitatively agree with simulated intensities plotted in Figure 2b. The measured wavelength dependence of the total power transmitted to free space confirms that the fundamental mode (Figure 3i) has the maximal transmission as a result of grating optimization. The Gaussian fit of the fundamental peak reveals  $\approx 90 \mu\text{m}$  fwhm (Figure 3g). The deviation from the designed value ( $\approx 118 \mu\text{m}$  fwhm) is due to fabrication imperfections, such as possibly slightly deeper or wider grating grooves. Hence, the mode size conversion ratio between the single-mode waveguide with cross-sectional dimensions of  $250 \text{ nm} \times 300 \text{ nm}$  and the projected Gaussian beam of  $90 \mu\text{m} \times$

$172 \mu\text{m}$  fwhm Gaussian beam is  $\approx 2.1 \times 10^5$ . The measured conversion efficiency of the fundamental resonance, defined as the total power from the grating measured in free-space relative to the waveguide power at the device, is  $\approx 4.5 \text{ dB}$ .

To quantify the free-space beam propagation, we acquire images of the outcoupled radiation (Figure 4a) in focal planes located at known distances within a few millimeters above and below the chip surface (Figure 4b). The beam's waist analysis based on the Gaussian fit for each image indicates that the radiation profile maintains its shape across at least 14 mm, indicating good collimation with minimal wavefront distortion (Figure 4c). The weak focusing observed above the chip surface is indicative of a small wavefront curvature, which is attributed to fabrication imperfections. By quantifying the lateral beam shift in the direction across the grating lines as a function of the focal plane height, we find that the beam emanates close to a surface normal at an average angle of  $0.06^{\circ+0.22^{\circ}}_{-0.07^{\circ}}$ . The reported uncertainties correspond to the minimum and maximum bounds, obtained by fitting the measured data within different  $z$ -coordinate subdomains in Figure 4c.

**Thermo-Optical Tuning.** Finally, we demonstrate how we leverage the thermo-optical effect to precisely tune the device to a desired operating wavelength. Due to its resonant nature, the optimal emission wavelength of this device is sensitive to fabrication imperfections and may deviate from the desired value. Thermo-optical tuning provides means to compensate for fabrication deficiencies. Figure 5 illustrates how the free-space intensity profiles at a single wavelength vary with increasing device temperature within the range of  $\approx 80 \text{ K}$  from the room temperature. Initially tuned into the fundamental mode at the room temperature, the free-space beam intensity pattern transitions to high-order modes upon heating. The conducted experiments confirm that the device tunability is fully reversible and repeatable. By comparing the intensity profiles, the temperature variation can be equated to an equivalent wavelength change, as shown in Figure 5; for example, heating the resonant grating by  $\approx 80 \text{ K}$  results in the same intensity profile change as tuning the wavelength by  $\Delta\lambda$

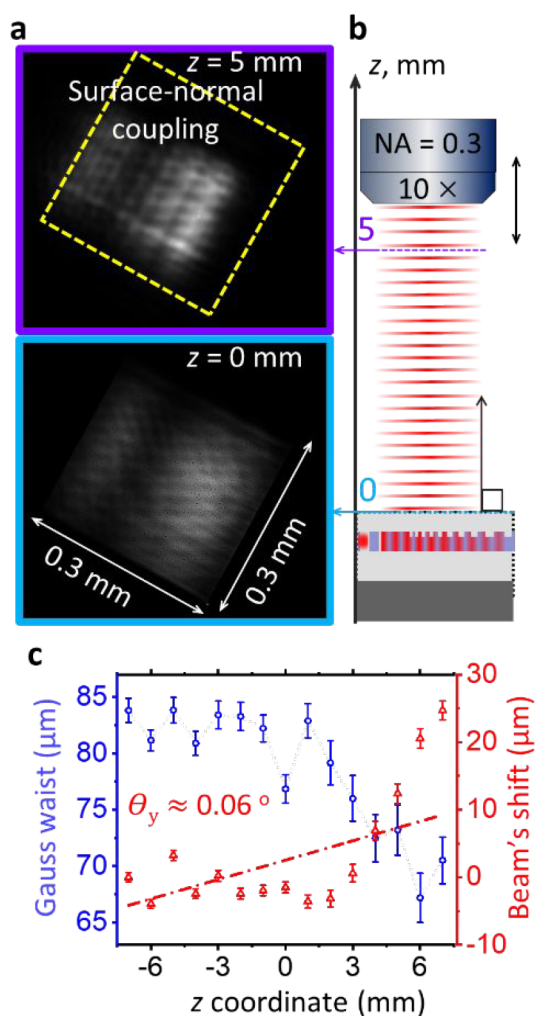


**Figure 4.** Characterization of the surface-normal free-space beam emanated from the grating coupler. (a) Free-space beam images acquired at focal planes at the chip surface (bottom image) and  $z = 5$  mm above the chip (top image). The grating is tuned into the fundamental mode ( $\lambda = 780.15 \pm 0.03$  nm). Yellow dashed box points out the position of the resonant grating. (b) A schematic showing image acquisition. (c) Evolution of the measured Gaussian waist and the lateral shift of the free-space Gaussian beam vs  $z$  coordinate. The outcoupling angle is estimated from the beam's shift as a function of the  $z$  coordinate. Dash-dot line is a linear fit of the beam's shift. Error bars correspond to one standard deviation of the data obtained from five equal image subdomains along the grating width.

$\approx 1$  nm. Linear fit to the data in Figure 5 indicates the wavelength tuning slope of  $0.012 \pm 0.001$  nm/K, with the one standard deviation uncertainty obtained from the fit parameter estimated variance.

## DISCUSSION

To summarize, we have demonstrated the deformation-based inverse design algorithm to optimize large photonic structures. The 300  $\mu\text{m}$  long grating projects a surface-normal 90  $\mu\text{m}$  fwhm collimated free-space beam from a photonic waveguide with high conversion efficiency. The unique performance of the novel photonic configuration is enabled due to spatially broad standing wave resonances, ensuring the surface-normal beam coupling due to an NZI operation. The slow-light grating modes ensure both the full mode matching minimizing reflection losses and free-space light intensity control. The

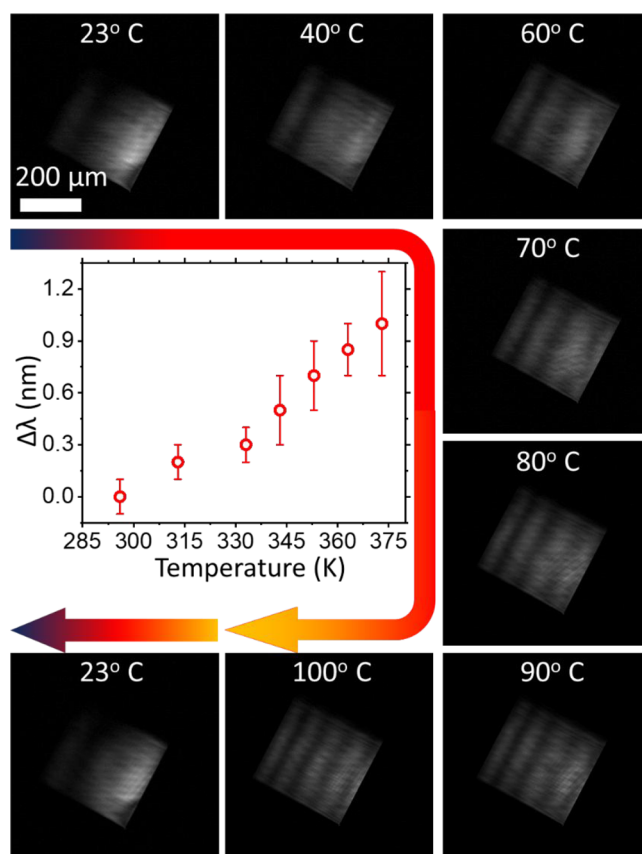


**Figure 5.** Thermo-optical tuning. Flowchart depicts the sequence of optical images of the projected free-space beam upon heating the resonant grating about 80 K above room temperature and then cooling back to room temperature.  $\Delta\lambda$  represents the estimated optimum wavelength tuning upon sample heating. Error bars represent uncertainties in wavelength detuning between two neighboring images for which the outcoupled free-space beam profile can be uniquely correlated to a specific temperature pattern.

experimentally realized photonic device is readily adaptable to operate at visible, telecom, and ultraviolet wavelengths and will further matchmake integrated photonics with free-space optics for novel chip-scale hybrid systems in science and technology realms with the immense need for planar 2D integration.

## MATERIALS AND METHODS

**Fabrication of the Photonic Chip.** The resonant gratings are realized using the standard nanofabrication techniques (see SI for details). A nominally 2.9  $\mu\text{m}$  thick  $\text{SiO}_2$  and 250 nm  $\text{SiN}_x$  continuous layers are formed using thermal oxidation and low-pressure chemical vapor deposition (LPCVD), respectively. Then electron-beam lithography and reactive-ion etching are employed twice to pattern fully etched high-confinement waveguides and evanescent expanders and 30 nm deep partially etched grating in the  $\text{SiN}_x$  slab. The top  $\approx 3$   $\mu\text{m}$  thick  $\text{SiO}_2$  cladding is deposited using LPCVD as well. All grating dimensions are thoroughly characterized using scanning electron microscopy.

**Characterization of the Device's Operation.** We utilize a fiber-coupled laser source tunable around 780 nm wavelength to feed the photonic chip and an optical microscope equipped with a 0.3 NA objective backed with a complementary metal oxide semiconductor (CMOS) camera to characterize the free-space beam profiles, respectively. Before conducting experi-

ments, we have calibrated the lasing wavelength by coupling to a commercial rubidium cell as a reference and also using a wavemeter. The characteristic Rb transitions occur close to the grating fundamental mode at 780 nm. We then tune the laser from the calibrated Rb transitions to the wavelength of the resonant grating fundamental mode using a high-repeatability scan stepper motor and check the lasing wavelength by a wavemeter. From calibration data, we estimate the wavelength uncertainty in our experiments due to mode hopping to be within  $\pm 0.03$  nm range, which represents one standard deviation statistical uncertainty of the calibrated lasing wavelength across the range from 778.3 to 781.3 nm. The laser radiation is coupled to a TE<sub>0</sub> waveguide single-mode via an inverted-taper. We use a fiber polarizer and an attenuator to adjust the polarization and power ( $\approx 1$  mW) of the input light, respectively. To characterize the direction of the free-space beam, we analyze optical images collected at the grating surface and a few millimeters above the chip.

## ■ ASSOCIATED CONTENT

### SI Supporting Information

The Supporting Information is available free of charge at <https://pubs.acs.org/doi/10.1021/acsp Photonics.2c00422>.

Multiple additional numerical modeling and experimental data, and brief descriptions of the device fabrication sequence and the experimental measurement setup. Data includes numerically modeled far-field patterns at multiple frequencies, nearfield intensity vs frequency, modeling and experimental data on temperature dependence, numerically computed band diagrams corresponding to specific grating locations, and modeled stored energy as a function of frequency (PDF)

## ■ AUTHOR INFORMATION

### Corresponding Author

Vladimir A. Aksyuk – Physical Measurement Laboratory, National Institute of Standards and Technology, Gaithersburg, Maryland 20899, United States; [orcid.org/0000-0002-9653-4722](https://orcid.org/0000-0002-9653-4722); Phone: (301) 975-2867; Email: [vladimir.aksyuk@nist.gov](mailto:vladimir.aksyuk@nist.gov)

### Authors

Alexander Yulaev – Physical Measurement Laboratory, National Institute of Standards and Technology, Gaithersburg, Maryland 20899, United States; Department of Chemistry and Biochemistry, University of Maryland, College Park, Maryland 20742, United States; [orcid.org/0000-0002-9225-3448](https://orcid.org/0000-0002-9225-3448)

Daron A. Westly – Physical Measurement Laboratory, National Institute of Standards and Technology, Gaithersburg, Maryland 20899, United States

Complete contact information is available at:

<https://pubs.acs.org/doi/10.1021/acsp Photonics.2c00422>

### Author Contributions

V.A.A. conceived the idea and directed the work. A.Y. and D.A.W. fabricated samples. A.Y. characterized the samples. A.Y. and V.A.A. contributed to the data interpretation. The manuscript was written through contributions of all authors. All authors have given approval to the final version of the manuscript.

## Funding

The work is supported in part by the NIST on a Chip program. Dr. Alexander Yulaev acknowledges support under the Professional Research Experience Program (PREP), administered through the Department of Chemistry and Biochemistry, UMD.

## Notes

The authors declare no competing financial interest.

## ■ ACKNOWLEDGMENTS

We would like to thank Dr. John Kitching and Dr. Matthew Hummon for discussing surface-normal emission from photonic circuits and its applications to miniature atomic vapor devices. The data produced in this study are available from the corresponding author upon reasonable request.

## ■ REFERENCES

- (1) Kippenberg, T. J.; Holzwarth, R.; Diddams, S. A. Microresonator-based optical frequency combs. *Science* **2011**, *332* (6029), 555–559.
- (2) Kitching, J.; Donley, E. A.; Knappe, S.; Hummon, M.; Dellis, A.; Sherman, J.; Srinivasan, K.; Aksyuk, V. A.; Li, Q.; Westly, D. NIST on a Chip: Realizing SI Units with Microfabricated Alkali Vapor Cells. *Journal of Physics: Conference Series* **2016**, *723*, 012056.
- (3) Grier, D. G. A revolution in optical manipulation. *Nature* **2003**, *424* (6950), 810.
- (4) Hummon, M. T.; Kang, S.; Bopp, D. G.; Li, Q.; Westly, D. A.; Kim, S.; Fredrick, C.; Diddams, S. A.; Srinivasan, K.; Aksyuk, V.; Kitching, J. E. Photonic chip for laser stabilization to an atomic vapor with 10-11 instability. *Optica* **2018**, *5* (4), 443–449.
- (5) Kohonen, M.; Succo, M.; Petrov, P.; Nyman, R.; Trupke, M.; Hinds, E. An array of integrated atom-photon junctions. *Nat. Photonics* **2011**, *5* (1), 35–38.
- (6) Mehta, K. K.; Bruzewicz, C. D.; McConnell, R.; Ram, R. J.; Sage, J. M.; Chiaverini, J. Integrated optical addressing of an ion qubit. *Nat. Nanotechnol.* **2016**, *11* (12), 1066.
- (7) Lin, S.; Crozier, K. B. Trapping-assisted sensing of particles and proteins using on-chip optical microcavities. *ACS Nano* **2013**, *7* (2), 1725–1730.
- (8) Xu, D. X.; Densmore, A.; Delage, A.; Waldron, P.; McKinnon, R.; Janz, S.; Lapointe, J.; Lopinski, G.; Mischki, T.; Post, E.; Cheben, P.; Schmid, J. H. Folded cavity SOI microring sensors for high sensitivity and real time measurement of biomolecular binding. *Opt. Express* **2008**, *16* (19), 15137–15148.
- (9) Sun, Y.; Fan, X. Optical ring resonators for biochemical and chemical sensing. *Anal. Bioanal. Chem.* **2011**, *399* (1), 205–211.
- (10) Squires, T. M.; Messinger, R. J.; Manalis, S. R. Making it stick: convection, reaction and diffusion in surface-based biosensors. *Nat. Biotechnol.* **2008**, *26* (4), 417–426.
- (11) Dantham, V.; Holler, S.; Kolchenko, V.; Wan, Z.; Arnold, S. Taking whispering gallery-mode single virus detection and sizing to the limit. *Appl. Phys. Lett.* **2012**, *101* (4), 043704.
- (12) Zhu, J.; Ozdemir, S. K.; Xiao, Y.-F.; Li, L.; He, L.; Chen, D.-R.; Yang, L. On-chip single nanoparticle detection and sizing by mode splitting in an ultrahigh-Q microresonator. *Nat. Photonics* **2010**, *4* (1), 46.
- (13) Thomson, D.; Zilkie, A.; Bowers, J. E.; Komljenovic, T.; Reed, G. T.; Vivien, L.; Marris-Morini, D.; Cassan, E.; Virot, L.; Fédéli, J.-M.; et al. Roadmap on silicon photonics. *Journal of Optics* **2016**, *18* (7), 073003.
- (14) Harris, J.; Winn, R.; Dalgoutte, D. Theory and design of periodic couplers. *Appl. Opt.* **1972**, *11* (10), 2234–2241.
- (15) Vedantam, S.; Lee, H.; Tang, J.; Conway, J.; Staffaroni, M.; Yablonovitch, E. A plasmonic dimple lens for nanoscale focusing of light. *Nano Lett.* **2009**, *9* (10), 3447–3452.

- (16) Yariv, A.; Yeh, P. *Photonics: optical electronics in modern communications (the oxford series in electrical and computer engineering)*; Oxford University Press, Inc., 2006.
- (17) Taillaert, D.; Bienstman, P.; Baets, R. Compact efficient broadband grating coupler for silicon-on-insulator waveguides. *Opt. Lett.* **2004**, *29* (23), 2749–2751.
- (18) Van Laere, F.; Roelkens, G.; Ayre, M.; Schrauwen, J.; Taillaert, D.; Van Thourhout, D.; Krauss, T. F.; Baets, R. Compact and highly efficient grating couplers between optical fiber and nanophotonic waveguides. *Journal of Lightwave Technology* **2007**, *25* (1), 151–156.
- (19) Roelkens, G.; Vermeulen, D.; Van Thourhout, D.; Baets, R.; Brison, S.; Lyan, P.; Gautier, P.; Fedeli, J.-M. High efficiency diffractive grating couplers for interfacing a single mode optical fiber with a nanophotonic silicon-on-insulator waveguide circuit. *Appl. Phys. Lett.* **2008**, *92* (13), 131101.
- (20) Mehta, K. K.; Ram, R. J. Precise and diffraction-limited waveguide-to-free-space focusing gratings. *Sci. Rep.* **2017**, *7* (1), 1–8.
- (21) Song, J. H.; Doany, F. E.; Medhin, A. K.; Dupuis, N.; Lee, B. G.; Libsch, F. R. Polarization-independent nonuniform grating couplers on silicon-on-insulator. *Opt. Lett.* **2015**, *40* (17), 3941–3944.
- (22) Kim, S.; Westly, D. A.; Roxworthy, B. J.; Li, Q.; Yulaev, A.; Srinivasan, K.; Aksyuk, V. A. Photonic waveguide to free-space Gaussian beam extreme mode converter. *Light: Science & Applications* **2018**, *7* (1), 72.
- (23) Yulaev, A.; Zhu, W.; Zhang, C.; Westly, D. A.; Lezec, H. J.; Agrawal, A.; Aksyuk, V. Metasurface-Integrated Photonic Platform for Versatile Free-Space Beam Projection with Polarization Control. *ACS Photonics* **2019**, *6* (11), 2902–2909.
- (24) Yulaev, A.; Zhu, W.; Zhang, C.; Westly, D. A.; Lezec, H. J.; Agrawal, A.; Aksyuk, V. High NA Free-Space Focusing Using a Metasurface-Integrated Photonic Platform for Atom Trapping. *CLEO: Applications and Technology*; Optical Society of America, 2019; p AM3K.2.
- (25) Chauhan, N.; Bose, D.; Puckett, M.; Moreira, R.; Nelson, K.; Blumenthal, D. J. Photonic integrated Si<sub>3</sub>N<sub>4</sub> ultra-large-area grating waveguide MOT interface for 3D atomic clock laser cooling. *2019 Conference on Lasers and Electro-Optics (CLEO)*; IEEE, 2019; pp 1–2.
- (26) Badham, K.; Kendrick, R. L.; Wuchenich, D.; Ogden, C.; Chriqui, G.; Duncan, A.; Thurman, S. T.; Yoo, S.; Su, T.; Lai, W. Photonic integrated circuit-based imaging system for SPIDER. *2017 Conference on Lasers and Electro-Optics Pacific Rim (CLEO-PR)*; IEEE, 2017; pp 1–5.
- (27) Michaels, A.; Yablonovitch, E. Inverse design of near unity efficiency perfectly vertical grating couplers. *Opt. Express* **2018**, *26* (4), 4766–4779.
- (28) Wang, B.; Jiang, J.; Nordin, G. P. Embedded slanted grating for vertical coupling between fibers and silicon-on-insulator planar waveguides. *IEEE Photonics Technology Letters* **2005**, *17* (9), 1884–1886.
- (29) Yin, X.; Jin, J.; Soljačić, M.; Peng, C.; Zhen, B. J. N. Observation of topologically enabled unidirectional guided resonances. *Nature* **2020**, *580* (7804), 467–471.
- (30) Baba, T. Slow light in photonic crystals. *Nat. Photonics* **2008**, *2* (8), 465–473.
- (31) Schulz, S.; O’Faolain, L.; Beggs, D. M.; White, T. P.; Melloni, A.; Krauss, T. F. Dispersion engineered slow light in photonic crystals: a comparison. *Journal of Optics* **2010**, *12* (10), 104004.
- (32) Notomi, M.; Yamada, K.; Shinya, A.; Takahashi, J.; Takahashi, C.; Yokohama, I. Extremely large group-velocity dispersion of line-defect waveguides in photonic crystal slabs. *Phys. Rev. Lett.* **2001**, *87* (25), 253902.
- (33) Magno, G.; Fevrier, M.; Gogol, P.; Aassime, A.; Bondi, A.; Mégy, R.; Dagens, B. Strong coupling and vortexes assisted slow light in plasmonic chain-SOI waveguide systems. *Sci. Rep.* **2017**, *7* (1), 1–11.
- (34) Gan, Q.; Fu, Z.; Ding, Y. J.; Bartoli, F. J. Ultrawide-bandwidth slow-light system based on THz plasmonic graded metallic grating structures. *Phys. Rev. Lett.* **2008**, *100* (25), 256803.
- (35) Huang, Y.; Min, C.; Veronis, G. Subwavelength slow-light waveguides based on a plasmonic analogue of electromagnetically induced transparency. *Appl. Phys. Lett.* **2011**, *99* (14), 143117.
- (36) Reshef, O.; Camayd-Muñoz, P.; Vulis, D. I.; Li, Y.; Lončar, M.; Mazur, E. Direct observation of phase-free propagation in a silicon waveguide. *ACS Photonics* **2017**, *4* (10), 2385–2389.
- (37) Li, Y.; Kita, S.; Muñoz, P.; Reshef, O.; Vulis, D. I.; Yin, M.; Lončar, M.; Mazur, E. On-chip zero-index metamaterials. *Nat. Photonics* **2015**, *9* (11), 738–742.
- (38) Liberal, I.; Engheta, N. Near-zero refractive index photonics. *Nat. Photonics* **2017**, *11* (3), 149–158.
- (39) Kinsey, N.; DeVault, C.; Boltasseva, A.; Shalaev, V. M. Near-zero-index materials for photonics. *Nature Reviews Materials* **2019**, *4*, 742–760.
- (40) Yulaev, A.; Kim, S.; Westly, D. A.; Roxworthy, B. J.; Li, Q.; Srinivasan, K. A.; Aksyuk, V. A. Collimating a Free-Space Gaussian Beam by Means of a Chip-Scale Photonic Extreme Mode Converter. *2018 International Conference on Optical MEMS and Nanophotonics (OMN)*; IEEE, 2018; pp 1–2.
- (41) Molesky, S.; Lin, Z.; Piggott, A. Y.; Jin, W.; Vucković, J.; Rodriguez, A. W. Inverse design in nanophotonics. *Nat. Photonics* **2018**, *12* (11), 659–670.
- (42) Piggott, A. Y.; Lu, J.; Lagoudakis, K. G.; Petykiewicz, J.; Babinec, T. M.; Vucković, J. Inverse design and demonstration of a compact and broadband on-chip wavelength demultiplexer. *Nat. Photonics* **2015**, *9* (6), 374–377.